PAPER

Accurate and Nonparametric Imaging Algorithm for Targets Buried in Dielectric Medium for UWB Radars

Ken AKUNE[†a)], *Student Member*, **Shouhei KIDERA**[†], *and* **Tetsuo KIRIMOTO**[†], *Members*

SUMMARY   Ultra-wide band (UWB) pulse radar with high range resolution and dielectric permeability is promising as an internal imaging technique for non-destructive testing or breast cancer detection. Various imaging algorithms for buried objects within a dielectric medium have been proposed, such as aperture synthesis, the time reversal approach and the space-time beamforming algorithm. However, these algorithms mostly require *a priori* knowledge of the dielectric medium boundary in image focusing, and often suffer from inadequate accuracy to identify the detailed structure of buried targets, such as an edge or specular surface owing to employing the waveform focusing scheme. To overcome these difficulties, this paper proposes an accurate and non-parametric (i.e. using an arbitrary shape without target modeling) imaging algorithm for targets buried in a homogeneous dielectric medium by advancing the RPM (Range Points Migration) algorithm to internal imaging issues, which has been demonstrated to provide an accurate image even for complex-shaped objects in free-space measurement. Numerical simulations, including those for two-dimensional (2-D) and three-dimensional (3-D) cases, verify that the proposed algorithm enhances the imaging accuracy by less than 1/10 of the wavelength and significantly reduces the computational cost by specifying boundary extraction compared with the conventional SAR-based algorithm.

key words: *UWB radars, non-destructive testing, RPM, accurate internal imaging*

1. Introduction

Ultra-wide band (UWB) pulse radar has great potential to determine the structure and location of an object buried in a human body or concrete wall, avoiding harm to human tissue or communication systems. Thus, this radar system is suitable for various sensing applications such as medical screening in the early-stage detection of breast tumors [1], non-destructive testing in the detection of cracks in pipes within walls [2], and the positioning of unexploded land mines buried in the subsurface [3]. Various internal imaging algorithms suitable for the above applications have been developed, such as synthetic aperture radar (SAR) [4] and the time reversal algorithm [5]. Recently, it was reported that microwave imaging via space-time (MIST) beamforming demonstrated significant potential in detecting tumors by removing scattered responses from breast surfaces to enhance detection accuracy in beamforming process [6], [7]. However, all the above algorithms usually require *a priori* knowledge of the dielectric medium boundary and cannot deal with the situation that the boundary is completely un-

known and has arbitrary shape. On the other hand, as accurate and non-parametric approaches to extract boundaries, a shape estimation algorithm based on BST (Boundary Scattering Transform) and extraction of directly scattered waves (SEABED), Envelope and range points migration (RPM) algorithm have been proposed [8]–[10] in the last decade, all of which basically employ a distinctive range obtained from an echo scattered on a clear target surface. In particular, it has been revealed that the RPM algorithm was able to accurately and robustly extract target boundaries, including those of complex-shaped or multiple objects, by exploiting the global feature of the range distribution.

As a simple solution to the problem faced by the conventional internal imaging algorithms, the combination of SAR and RPM is easily conceivable, and it is regarded as an extension to the previously published algorithm [11], employing double scattered signals for image expansion. While this algorithm is applicable to an unknown dielectric medium boundary, it is based on signal integration, and reproduces a blurred image for the object boundary. Its imaging accuracy is thus often insufficient to identify the detailed structure of buried objects, such as an edge or clear surface. In addition, this approach has an impractically high computational burden, especially for obtaining the full three-dimensional (3-D) target structure.

With this background as a substantial solution to the aforementioned problems, this paper extends the principle of the former RPM algorithm to internal imaging issues with the aim of enhancing imaging accuracy by specifying clear boundary extraction. The proposed algorithm is notable in that it efficiently employs dielectric boundary points and their normal vectors preliminarily obtained by RPM in estimating the propagation path, and it accurately extracts the internal target boundary points employing the advanced RPM principle derived from Snell's law under the condition of a homogeneous dielectric medium with known permittivity. The main advantage of our proposed algorithm is that it can deal with situations including an arbitrary dielectric medium boundary, and achieves imaging accuracy beyond the wavelength scale, which is adequate to specify the detailed shape of a target.

This paper first describes the conventional and proposed methodologies employed in constructing a two-dimensional (2-D) model, and validates the performance of each methodology in typical target cases and noisy situations. Subsequently, the extension of the 3-D model and its performance are presented. The results obtained from
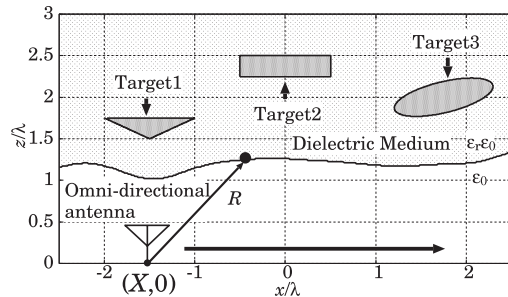
Fig. 1 System model.

numerical simulations in using the 2-D and 3-D models verify that our proposed algorithm provides non-marginal improvement in terms of accurate target boundary extraction, compared with the conventional SAR-based algorithm. Furthermore, the results verify that the proposed algorithm remarkably decreases the computational burden of internal imaging by avoiding integration.

2. System Model

Figure 1 shows the system model. It is assumed that the target is completely buried in a homogeneous dielectric medium, and both boundaries have arbitrary shapes, corresponding to a non-parametric issue. The relative permittivity of the dielectric medium is assumed to be given. A mono-static radar with an omni-directional antenna scans along the x-axis. A mono-cycle pulse whose central wavelength is denoted λ, is provided as a transmitting current waveform. The real space in which the target and antenna are located is defined by the parameters $r = (x, z)$. $s(X, R)$ is defined as the output of the matched filter at the antenna location $(X, 0)$, where $R = ct/2$ is expressed by time t and the propagation speed of the radio wave in air as c; the detailed procedure is described in the literature [10]. A set of range points denoted $Q \equiv \{q_i = (X_i, R_i), (i = 1, ...N_Q)\}$ is extracted from the local maxima of $s(X, R)$ [10].

3. Conventional Algorithm

Various internal imaging algorithms have been developed, most of which are based on SAR, time reversal approach or a beamforming scheme. However, these algorithms basically require a certain level of *a priori* information about the shape of the dielectric boundary, and such information is not always available in practical situations. As a solution to this problem, this paper introduces the extended algorithm of [11], that originally aims at image expansion employing double scattered component, to internal imaging issue as the suitable conventional technique. The algorithm [11] is easily extended to an internal imaging algorithm by employing RPM target points for dielectric boundary extraction and aperture synthesis considering the velocity degradation in a dielectric medium.

The methodology of the algorithm is briefly explained as follows. The algorithm deals with the boundary points of

the dielectric medium $r_{S,j} = (x_{S,j}, z_{S,j}) (j = 1, ..., N_S)$, preliminarily produced by the RPM algorithm with a subset of Q denoted $Q_S \equiv \{q_{S,j} = (X_{S,j}, R_{S,j}), (j = 1, ..., N_S)\}$, with each member having a minimum R for each antenna location. This algorithm regards each point $r_{S,j}$ as a candidate for an incident point on the dielectric medium boundary. The SAR scheme is then incorporated into the imaging of a target buried in a dielectric medium using RPM points. If the relative permittivity ϵ_r is known, the internal image $I(r)$ is formulated as

$$I(r) = \int_{X \in \Gamma} \sum_{j=1}^{N'_S} s(q_{S,j}) s(X, d_2(X, r, r_{S,j})) dX, \qquad (1)$$

where Γ denotes the spatial range of the antenna scanning. $d_2(X, r, r_{S,j}) = \sqrt{(X - x_{S,j})^2 + z_{S,j}^2} + \sqrt{\epsilon_r} \sqrt{(x - x_{S,j})^2 + (z - z_{S,j})^2}$. $r_{S,j}$ is interpolated with an envelope [9] of circles whose center is $(X_{S,j}, 0)$ and radius is $R_{S,j}$, and this interpolation process increases the number of boundary points to N'_S to obtain an adequate area for the incident boundary. In Eq. (1), a buried target boundary is reconstructed by aperture synthesis considering velocity degradation.

Here, one numerical example is presented for the problem statement of this algorithm, where the received signals are calculated in the finite-difference time domain (FDTD). In this FDTD simulation, the time step interval is set to $1/200$T and the spatial cell size is $1/80\lambda$, where T $= \lambda/c$. A mono-cycle pulse with a fractional bandwidth (FBW) of approximately 140% is provided as a current waveform, which satisfies the definition of UWB signals in FCC (Federal Communications Commission). A Mur second-order absorbing boundary is adopted in this case. Since this boundary condition does not match the lossy dielectric medium, there is a small reflection signal from the numerically truncated boundary particularly within the dielectric medium. However, this simulation provides some redundant space in the medium where the response of the internal target boundary and the reflection from the numerically truncated boundary do not interfere significantly. In particular, the spatial size of the FDTD simulation is set to $-3.5\lambda \leq x \leq 3.5\lambda$ and $0\lambda \leq z \leq 3.5\lambda$ to avoid the such interference, where the internal target boundary exists within $-2.5\lambda \leq x \leq 2.5\lambda$, $0\lambda \leq z \leq 3.0\lambda$. Figure 2 presents the output of the matched filter as $s(X, R)$ and the extracted range points Q_S in case (a) illustrated in Fig. 1, where each signal is received at 101 locations for $-2.5\lambda \leq X \leq 2.5\lambda$. Figure 3 also shows one sample from Fig. 2 at $X = -1\lambda$, where the reflected echoes from the dielectric and internal targets are sequentially received at each time of arrival. The conductivity of each target is set to 1.0×10^6 S/m. The conductivity and relative permittivity of the dielectric medium are set to 1.0×10^{-2} S/m and $\epsilon_r = 5.0$, respectively. Figure 4 shows the image $I(r)$ obtained by this algorithm in the noiseless situation, where the amplitude of $I(r)$ is normalized by the maximum value of $I(r)$. Here, $N'_S = 501$. It is confirmed that while parts of the internal
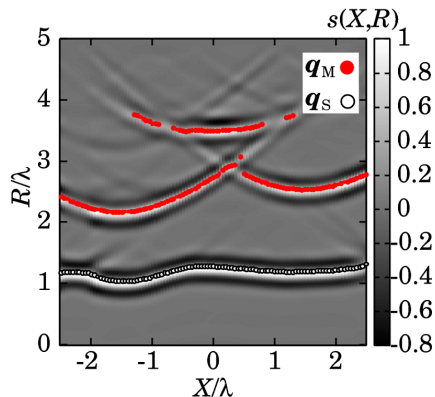
Fig. 2 Output of the matched filter $s(X, R)$, where the target as in Fig. 1 is assumed.
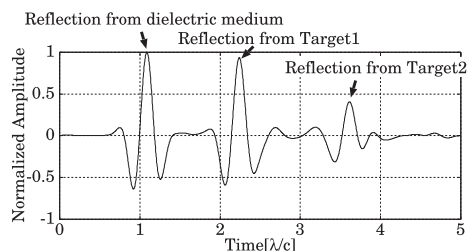
**Fig. 3** Output waveform of the matched filter, where $(X, 0) = (-1\lambda, 0)$.
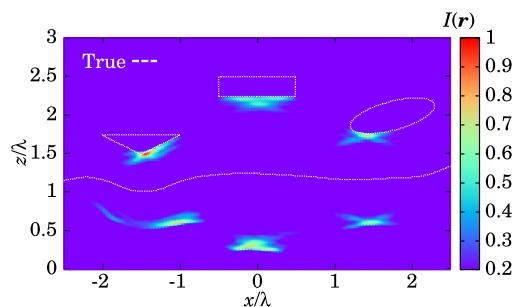
Fig. 4 Estimated images with the conventional SAR-based algorithm in noiseless situation:case (a).

target boundaries can be reproduced, undesirable false images are created especially below the dielectric medium. It is also seen that the algorithm does not offer sufficient accuracy to identify the structure of a distinctive target, such as an edge or clear surface. Furthermore, the computational time is around 950 sec in the case of Fig. 4 when using a Xeon 2.40 GHz processor. In the three-dimensional case, it is easily to predict that the computational cost will increase to a high level that is impractical for applications to medical screening and non-destructive testing.

4. Proposed Algorithm

To overcome the problems described above, this paper proposes a novel non-parametric imaging algorithm for objects buried in a dielectric medium. The algorithm makes use
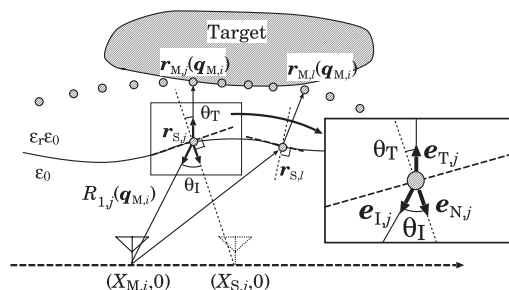
Fig. 5 Relationship between the potential target points and the boundary points of the dielectric medium.

of the inherent characteristics of the RPM algorithm, which can provide not only accurate target points but also their normal vectors on the target boundary without employing the spatial differential approach. This property is a distinct advantage because, if a normal vector at each dielectric boundary point is given, the propagation path in the medium is simply calculated using Snell's law. In fact, each normal vector at RPM boundary points $r_{\mathrm{S},j}$ is calculated as $e_{\mathrm{N},j} = \left(\left(X_{\mathrm{S},j} - x_{\mathrm{S},j} \right), -z_{\mathrm{S},j} \right) / R_{\mathrm{S},j}$. This formulation is derived from the well-established principle that each antenna receives a strong echo from the surface perpendicular to the line of sight [10].

Here, a set of all range points except Q_{S} is denoted $Q_{\mathrm{M}} = Q \cap \overline{Q_{\mathrm{S}}} \equiv \left\{ q_{\mathrm{M},i} = (X_{\mathrm{M},i}, R_{\mathrm{M},i}), (i = 1, ..., N_{\mathrm{M}}) \right\}$. For each $r_{\mathrm{S},j}$, the potential target points $r_{\mathrm{M},j} \left(q_{\mathrm{M},i} \right)$ corresponding to $q_{\mathrm{M},i}$ are calculated:

$$r_{\mathrm{M},j} \left(q_{\mathrm{M},i} \right) = r_{\mathrm{S},j} + \frac{\left(R_{\mathrm{M},i} - R_{1,j} \left(q_{\mathrm{M},i} \right) \right) e_{\mathrm{T},j}}{\sqrt{\epsilon_{\mathrm{r}}}}, \quad (2)$$

where $R_{1,j} \left(q_{\mathrm{M},i} \right) = \sqrt{\left(X_{\mathrm{M},i} - x_{\mathrm{S},j} \right)^2 + z_{\mathrm{S},j}^2}$, $e_{\mathrm{T},j} = \mathbf{R} \left(\theta_{\mathrm{T}} \right) \left(-e_{\mathrm{N},j} \right)$ and $\mathbf{R}(\theta)$ is a rotation matrix in the counterclockwise direction, and the refraction angle $\theta_{\mathrm{T}} = \sin^{-1} \left(\sin \theta_{\mathrm{I}} / \sqrt{\epsilon_{\mathrm{r}}} \right)$. The incident angle is denoted by $\theta_{\mathrm{I}} = \sin^{-1} \left(e_{\mathrm{N},j} \times e_{\mathrm{I},j} \right)$, where $e_{\mathrm{I},j} = \left(\left(X_{\mathrm{M},i} - x_{\mathrm{S},j} \right), -z_{\mathrm{S},j} \right) / R_{1,j} \left(q_{\mathrm{M},i} \right)$. Figure 5 shows the relationship between the potential target points and the boundary points of the dielectric medium.

The algorithm assumes that the target point exists in a set of $r_{\mathrm{M},j} \left(q_{\mathrm{M},i} \right)$. To detect the actual target point corresponding to $q_{\mathrm{M},i}$, a function $f \left(r_{\mathrm{M},j} \left(q_{\mathrm{M},i} \right), q_{\mathrm{M},k} \right)$ is introduced:

$$f \left(r_{\mathrm{M},j} \left(q_{\mathrm{M},i} \right), q_{\mathrm{M},k} \right)$$
$$= \exp \left(- \frac{\min\limits_{1 \le l \le N'_{\mathrm{S}}} \left| r_{\mathrm{M},j} \left(q_{\mathrm{M},i} \right) - r_{\mathrm{M},l} \left(q_{\mathrm{M},k} \right) \right|^2}{2\sigma_r^2} \right), \quad (3)$$

where σ_r is an empirically determined constant. Figure 6 depicts the relationship between the two groups of candidate points $r_{\mathrm{M},j} \left(q_{\mathrm{M},i} \right)$ and $r_{\mathrm{M},l} \left(q_{\mathrm{M},k} \right)$. Any function with a
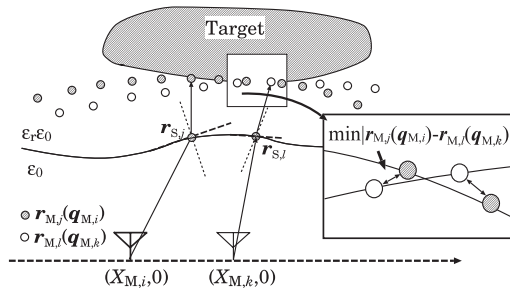
Fig. 6 Relationship between the two groups of the potential points $r_{M,j}\left(q_{M,i}\right)$ and $r_{M,l}\left(q_{M,k}\right)$.

central peak and symmetric curve, such as the raised cosine function, can be used in Eq. (3) instead of the Gaussian function. $f\left(r_{M,j}\left(q_{M,i}\right), q_{M,k}\right)$ is a weight based on the minimum distance between $r_{M,j}\left(q_{M,i}\right)$ and all candidate points determined by $q_{M,k}$. The principle of this algorithm is that the intersection point between the target candidate's curves $r_{M,j}\left(q_{M,i}\right)$ and $r_{M,l}\left(q_{M,k}\right)$ converge around the actual target boundary when $X_{M,k} \rightarrow X_{M,i}$, and this can be regarded as the extended principle of the RPM [10]. The evaluation function for each $q_{M,i}$ is then introduced as:

$$F\left(r_{M,j}\left(q_{M,i}\right); q_{M,i}\right) = \sum_{k=1}^{N_M} s\left(q_{M,k}\right) f\left(r_{M,j}\left(q_{M,i}\right), q_{M,k}\right)$$

$$\times \exp\left(-\frac{\left|X_{M,i} - X_{M,k}\right|^2}{2\sigma_X^2} - \frac{\left|R_{M,i} - R_{M,k}\right|^2}{2\sigma_R^2}\right), \quad (4)$$

where σ_X and σ_R are empirically determined constants. $\exp(*)$ in the right term of Eq. (4) denotes the weight, considering the scattered center shift in terms of antenna location, and focusing on neighboring range points. Finally, the target point for each $q_{M,i}$ is calculated as

$$\hat{r}_M\left(q_{M,i}\right) = \underset{r_{M,j}\left(q_{M,i}\right)}{\arg\max} \left|F\left(r_{M,j}\left(q_{M,i}\right); q_{M,i}\right)\right|. \quad (5)$$

It is expected that our algorithm realizes accurate internal imaging by incorporating the principle of the RPM algorithm and Snell's law.

The actual procedure of the proposed algorithm is summarized as follows:

Step 1)   The boundary points of the dielectric medium are obtained by RPM [10], where the sparse area of the boundary is interpolated by the envelope of circles defined by Q_S [9].

Step 2)   A set of the potential target points for each range point $q_{M,i}$ is obtained as $r_{M,j}\left(q_{M,i}\right)$ in Eq. (2).

Step 3)   The estimated target point $\hat{r}_M\left(q_{M,i}\right)$ is obtained by optimizing the evaluation function in Eq. (5).

Step 4)   Steps 2) and 3) are carried out for all range

points in Q_M, and a tentative set of target points denoted $\mathcal{T}^{pro}$ is obtained.

Step 5)   A target point is removed from $\mathcal{T}^{pro}$ as a false image, that satisfy,

$$F\left(r_{M,j}\left(q_{M,i}\right); q_{M,i}\right) \leq \beta \max_i F\left(r_{M,j}\left(q_{M,i}\right); q_{M,i}\right). \quad (6)$$

β is empirically determined.

Step 5) can suppress the false images caused by random noise, because the evaluation function $F\left(r_{M,j}\left(q_{M,i}\right); q_{M,i}\right)$ insufficiently grows in the case in which the range points are randomly distributed.
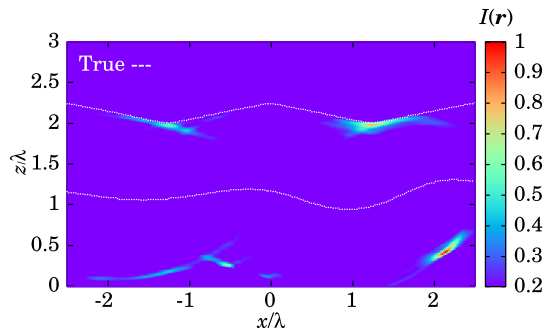
5.   Performance Evaluation of the Numerical Simulation

This section presents examples of the use of the proposed algorithm. Figure 7 shows the target points estimated by RPM and the proposed algorithm in case (a) using the same data as in Fig. 2. $\sigma_r = 0.1\lambda$, $\sigma_X = 0.75\lambda$, $\sigma_R = 0.5\lambda$ and $\beta = 0.3$ are set. Here, the black points denote the target points obtained by the proposed algorithm and the white points are those preliminarily estimated by the RPM algorithm and Envelope interpolation, where $N'_S = 501$. Figure 7 shows that the proposed algorithm accurately reconstructs the lower side of each object including the edge of a triangular object, and the false images outside the dielectric boundary are completely suppressed. It should be noted that the right side of the elliptical target is not reproduced in this case, because the reflection signal around this region cannot be obtained in the assumed observation region. The computational time is less than 40 sec when using a Xeon 2.40 GHz processor. In addition, the required computational complexity for each algorithm is $O\left(N_X^2 N_x N_z\right)$ for the conventional SAR-based algorithm and $O\left(N_X^3\right)$ for the proposed algorithm, where N_X, N_x and N_z denote the sampling numbers of X, x and z, respectively, and $O(*)$ gives the Landau notation. Here, we set $N_X = 101$, $N_x = 401$, $N_z = 241$, and the computational complexity of the proposed algorithm improves by a factor of 25 compared with that of the conventional algorithm. This verifies that the proposed algorithm significantly decreases the computational burden, compared with the conventional SAR-based algorithm, by removing the waveform integration for each imaging pixel.

Next, an example of a noisy situation is investigated. The upper graph in Fig. 8 shows the estimated points obtained by the RPM and by the proposed algorithm in case (a), at S/N=20 dB. Here, Gaussian white noise is added to the received signals and the signal to noise ratio is defined as the ratio of the peak instantaneous signal power to the average noise power after applying the matched filter. The upper graph in Fig. 8 indicates that although a few points deviate from the actual boundary, the proposed algorithm still maintains good accuracy in this situation. This is because the evaluation function in Eq. (4) does not significantly grow
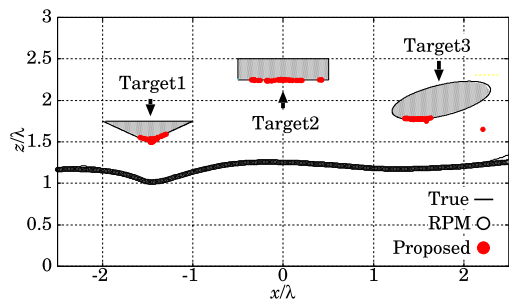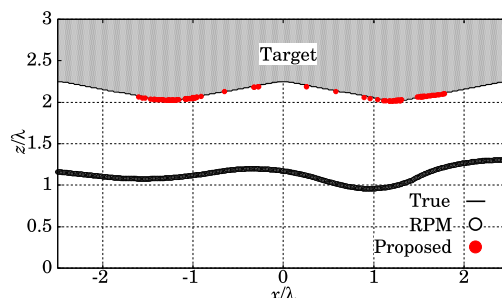
Fig. 7 Estimated image with the proposed algorithm in noiseless situation:case (a).
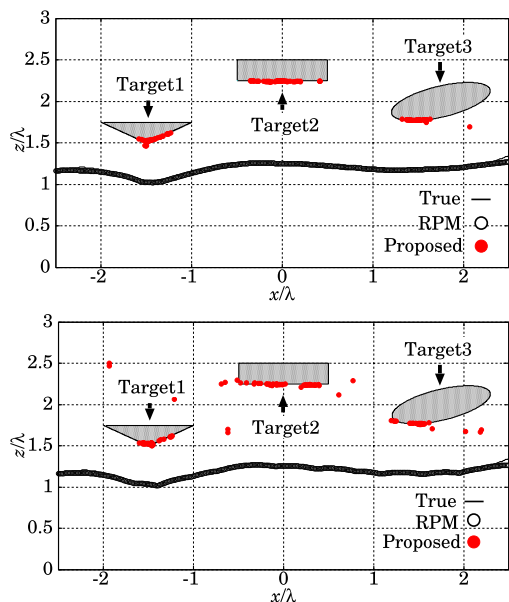
Fig. 8 Estimated image with the proposed algorithm in noisy situation:case(a) (upper:S/N=20 dB, lower:S/N=10 dB).

Fig. 9 Estimated images with the conventional SAR-based algorithm in noiseless situation:case (b).

Fig. 10 Estimated image with the proposed algorithm in noiseless situation:case (b).

since the neighboring range points around the false range are randomly distributed, and this component is removed in Eq. (6). In addition, the lower graph in Fig. 8 illustrates the noisier situation of S/N=10 dB in case (a), and shows that while the estimated dielectric surface obtained by RPM fluctuates with noise, most of the estimated points are located accurately around the actual target boundary. This result indicates that the proposed algorithm is not so sensitive to estimation errors for the dielectric surface, because each normal vector is not calculated by differential operation on the dielectric boundary but is rather determined from the fact that the target boundary should be perpendicular to the line of sight from the antenna location [10].

To validate the versatility of the proposed algorithm, another target case, which is called "case (b)", is investigated. Figures 9 and 10 represent the images obtained by the conventional and proposed algorithm in the noiseless situation in case (b), where the parameters are the same as those used in case (a) shown in Figs. 4 and 7, respectively. Figure 9 shows that even though the two convex edge regions are in focus, the image obtained by the conventional algo-

rithm is not clear enough to identify the target structure, and there are strong false images below the dielectric medium boundary. On the contrary, Fig. 10 demonstrates that the proposed algorithm has a sufficient accuracy to observe an edge or smooth clear surface around a convex region of the target. However, the area around the concave boundary is sparsely reconstructed because the direct scattered signal cannot be obtained around this region. In addition, the upper and lower graphs in Fig. 11 show the images estimated by the proposed algorithm in two noisy situations, where S/N=20 dB and S/N=10 dB, respectively. While most of the estimated target points for S/N=20 dB are accurate, in the case of S/N=10 dB, there are a number of points far from the actual target boundary, which is mainly caused by the noisy components.
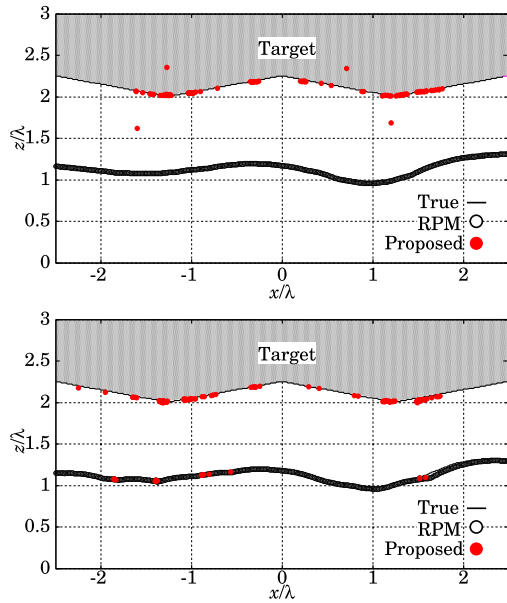
5.1 Quantitatively Analysis

For quantitative analysis of an obtained internal image, an evaluation value is introduced as
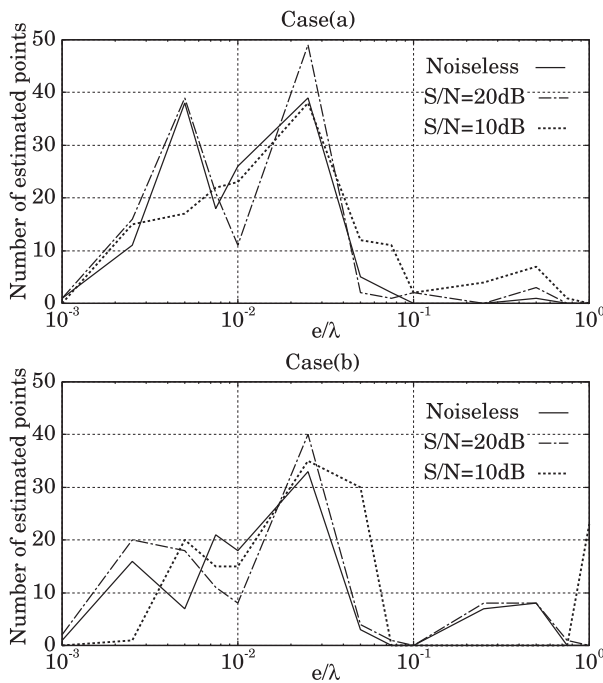
$$\mathrm{e}\left(\boldsymbol{q}_{\mathrm{M},i}\right) = \min_{\boldsymbol{r}_{\mathrm{true}}} \left\|\hat{\boldsymbol{r}}_{\mathrm{M}}\left(\boldsymbol{q}_{\mathrm{M},i}\right) - \boldsymbol{r}_{\mathrm{true}}\right\|, (i = 1, 2, ..., N_{\mathrm{M}}). \quad (7)$$

Here, $\boldsymbol{r}_{\mathrm{true}}$ expresses the location of the true target point. The upper and lower graphs in Fig. 12 show the number of estimated points for each value of $\mathrm{e}\left(\boldsymbol{q}_{\mathrm{M},i}\right)$ in both case (a) and case (b). The figure reveals that almost all the estimated points follow $\mathrm{e}\left(\boldsymbol{q}_{\mathrm{M},i}\right) \leq 10^{-1}\lambda$. Also, Table 1 presents the mean accuracy $\bar{\mathrm{e}}$ of $\mathrm{e}\left(\boldsymbol{q}_{\mathrm{M},i}\right)$ in each target case. Here, the mean accuracy in the case (b) becomes worse than that in

Fig. 11 Estimated image with the proposed algorithm in noisy situation:case (b) (upper:S/N=20 dB, lower:S/N=10 dB).
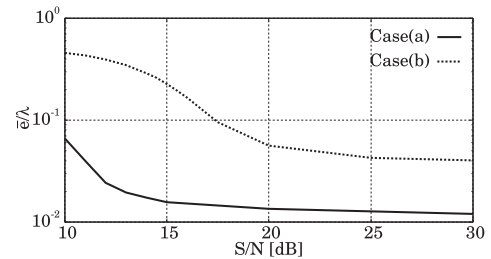

Fig. 12 Number of the estimated target points in noiseless situation and noisy situation (upper:case (a), lower:case (b)).

Table 1 Mean accuracies $\bar{e}$ for each target case.

	Case(a)	Case(b)
Noiseless	$1.28 \times 10^{-2}\lambda$	$3.73 \times 10^{-2}\lambda$
S/N = 20 dB	$1.68 \times 10^{-2}\lambda$	$4.90 \times 10^{-2}\lambda$
S/N = 10 dB	$8.78 \times 10^{-2}\lambda$	$2.05 \times 10^{-1}\lambda$

Fig. 13 Relationship between the mean accuracy and S/N for each case.
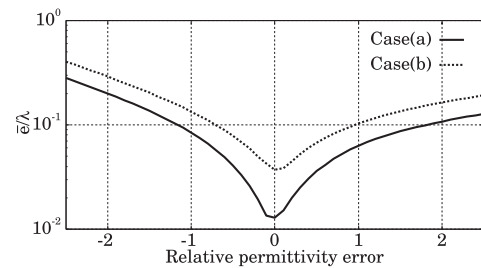
Fig. 14 Relationship between the mean accuracy and the error in the relative permittivity for each case.

gorithm maintains the accuracy within 0.1 λ in both cases, which is sufficient to identify the target shape in most cases.

Furthermore, for validation in a more practical situation, the sensitivity to permittivity error is investigated. Figure 14 depicts the relationship between $\bar{e}$ and the error in the relative permittivity, which at $\epsilon_r = 5.0$ varies from the true relative permittivity by between -2.5 and +2.5 for both case (a) and case (b). Here, we assume the situation is noiseless. The figure verifies that the proposed algorithm maintains the accuracy within 0.1λ between -1.0 and +1.0. In an actual imaging scene, while this algorithm needs to be combined with the permittivity estimation algorithm, this result demonstrates that the proposed algorithm can permit a certain level of permittivity error.

5.2 Performance Evaluation in Inhomogeneous Medium

The performance evaluation for targets in an inhomogeneous medium is presented to assess the applicability of this algorithm. The relative permittivity distribution given by the Gaussian distribution is shown in Fig. 15, where the standard deviation of ϵ_r is 5.54×10^{-1} and its mean value is 5.02. The conductivity is set to 0.01 S/m for simplicity. The true target and dielectric medium boundaries used are the same as in case (a). Figure 16 illustrates the estimated image at S/N=20 dB, while Fig. 17 shows the number of estimated points for each value of $e\left(\boldsymbol{q}_{\text{M},i}\right)$ compared to the
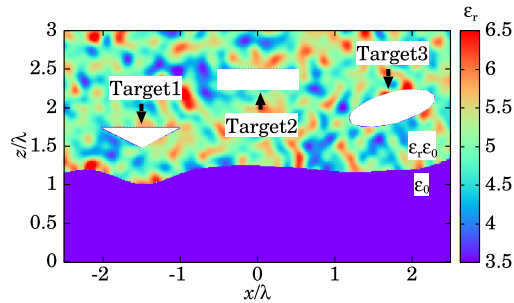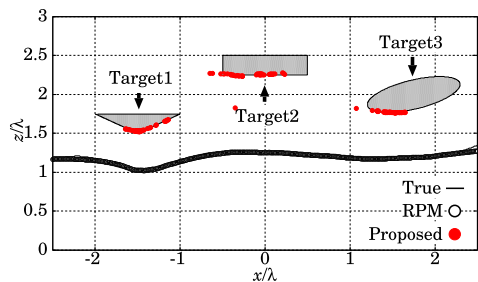
the case of (a) because false images are created by multiple scattered components, which cannot be removed in Eq. (6). It is our future work to eliminate such false images taking an approach such as those described in [8] and [12]. From a statistical viewpoint, Fig. 13 illustrates the relationship between $\bar{e}$ and S/N for both case (a) and case (b), where nine different types of noises are tested for each S/N. The figure shows that in the case of S/N $\geq$ 20 dB, the proposed al-

Fig. 15 Relative permittivity distribution in the inhomogeneous medium: case(a).

**Fig. 16** Estimated image with the proposed algorithm in the inhomogeneous medium in S/N=20 dB:case(a).
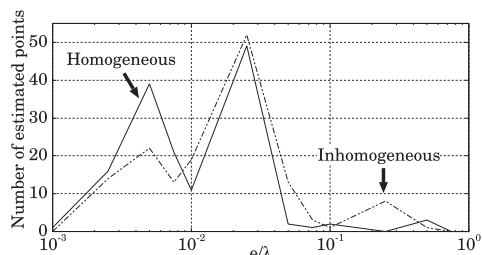
Fig. 17 Number of the estimated target points in the inhomogeneous medium in S/N=20 dB:case(a).

homogeneous case at S/N=20 dB. These results shows that, while the imaging accuracy is affected by permittivity fluctuations, the proposed algorithm can provide a significant image of the internal target boundary because the estimated propagation path is not considered to be far from the actual one.

6. Extension to 3-D Problems

6.1 System Model

Figure 18 shows the system model in a 3-D model. The target and dielectric medium model, antenna, and transmitted signal are assumed to be the same as those for the 2-D model. The antenna is scanning on the $z = 0$ plane. Additionally, linear polarization in the direction of the x-axis is assumed. Real space is expressed by the parameters $\boldsymbol{r} = (x, y, z)$. $z > 0$ is assumed for simplicity. $s'(X, Y, R)$ denotes the electric field received at the antenna location $(x, y, z) =$
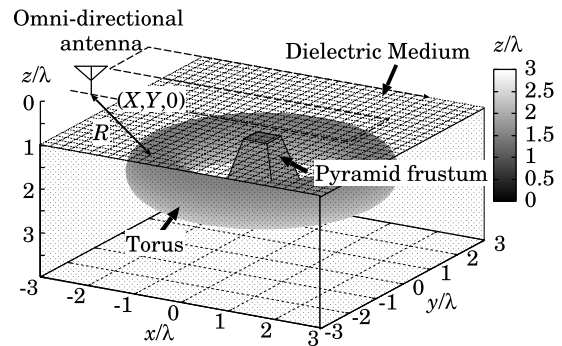
Fig. 18 System model in 3-D problem.

$(X, Y, 0)$. $s(X, Y, R)$ denotes the output of the matched filter. Range points $Q \equiv \{\boldsymbol{q}_i = (X_i, Y_i, R_i), (i = 1, \ldots N_Q)\}$ are obtained employing the same procedure described in Sect. 2.

6.2 Proposed Algorithm

The extension of the proposed algorithm to the 3-D problem is presented here. As in the case of the 2-D model, the algorithm exploits accurate target points and normal vectors on the boundaries created by the RPM, for which the 3-D model has been already derived [10]. We focus on a different part from the 2-D model for the proposed algorithm. As mentioned in Step 1) in Sect. 4, the potential target points for internal imaging can be densely interpolated if an adequate interpolation interval for the dielectric boundary is obtained by the Envelope in the 3-D version [13]. However, with a 3-D problem, the large number of potential target points requires a huge amount of calculation, and so there is a serious trade-off between the computational time and the accuracy. To avoid this trade-off, the following evaluation function in Eq. (3) for $\boldsymbol{q}_{M,i}$ is introduced as

$$f\left(\boldsymbol{r}_{M,j}\left(\boldsymbol{q}_{M,i}\right), \boldsymbol{q}_{M,k}\right)$$
$$= \exp\left(-\frac{\left|d_{\min}\left(\boldsymbol{r}_{M,j}\left(\boldsymbol{q}_{M,i}\right), \boldsymbol{r}_{M,l}\left(\boldsymbol{q}_{M,k}\right)\right)\right|^2}{2\sigma_r^2}\right), \quad (8)$$

where $d_{\min}$ denotes the minimum distance between $\boldsymbol{r}_{M,j}\left(\boldsymbol{q}_{M,i}\right)$ and the plane determined by the three potential points corresponding to $\boldsymbol{q}_{M,k}$, which are closest to $\boldsymbol{r}_{M,j}\left(\boldsymbol{q}_{M,i}\right)$. Figure 19 shows the relationship between $\boldsymbol{r}_{M,j}\left(\boldsymbol{q}_{M,i}\right)$ and other potential points obtained from $\boldsymbol{q}_{M,k}$ and the minimum distance $d_{\min}$. The evaluation function $F\left(\boldsymbol{r}_{M,j}\left(\boldsymbol{q}_{M,i}\right); \boldsymbol{q}_{M,i}\right)$ and the actual points $\hat{\boldsymbol{r}}_M\left(\boldsymbol{q}_{M,i}\right)$ are then determined using the same procedure used for the 2-D model employing Eqs. (4) and (5).

6.3 Performance Evaluation in Numerical Simulation

This section presents an application example of the proposed algorithm. Figure 20 shows the points estimated using the proposed algorithm and RPM algorithm for S/N ≥

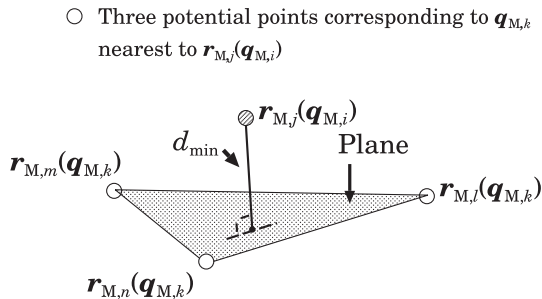○ Three potential points corresponding to $\boldsymbol{q}_{\mathrm{M},k}$ nearest to $\boldsymbol{r}_{\mathrm{M},j}(\boldsymbol{q}_{\mathrm{M},i})$

Fig. 19 Relationship between $\boldsymbol{r}_{\mathrm{M},j}\left(\boldsymbol{q}_{\mathrm{M},i}\right)$ and $d_{\min}$.
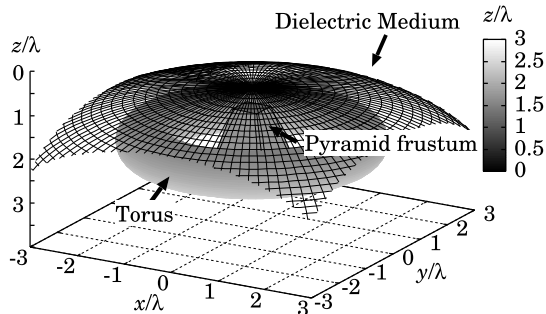

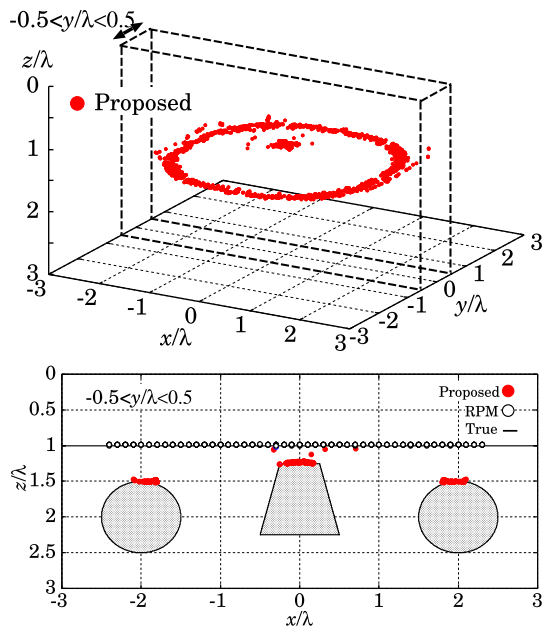**Fig. 21** True ellipsoidal surface and target boundary.

Fig. 20 Estimated target points with the proposed algorithm for the 3-D targets in S/N=25 dB.
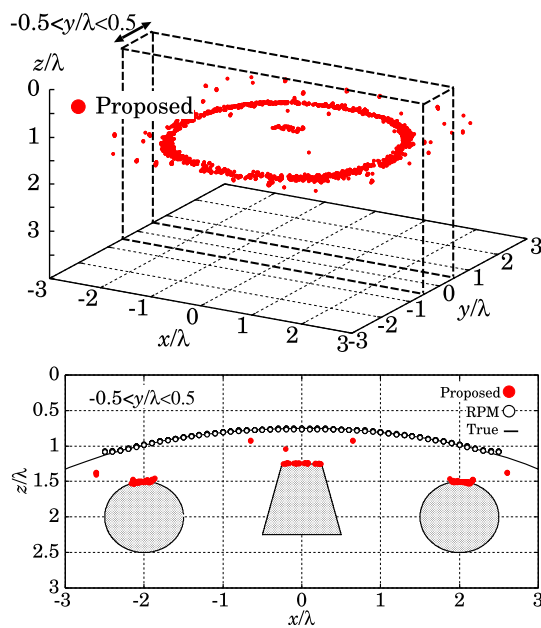

Fig. 22 Estimated target points with the proposed algorithm for the 3-D targets in S/N=25 dB.

25 dB, where the signal to noise ratio is defined the same as for the 2-D model. The target boundary is assumed as in Fig. 18, where the conductivity of each target is set to 1.0×10^6 S/m, and the conductivity and relative permittivity of the dielectric medium are set to 1.0×10^{-2} S/m and $\epsilon_{\mathrm{r}} = 5.0$, respectively. The mono-static radar is scanned over $-2.5\lambda \le x, y \le 2.5\lambda$, where the number of locations on each axis is 51. $\sigma_r = 0.1\lambda$, $\sigma_X = 0.5\lambda$, $\sigma_R = 0.5\lambda$ and $\beta = 0.6$ are set. Here, $N'_{\mathrm{S}} = 2601$. The figure verifies that the proposed algorithm achieves accurate target point estimation for the lower side of the torus and pyramid frustum.

As a further example, we investigate the ellipsoidal dielectric surface shown in Fig. 21, where the embedded target shapes and locations are the same as in the previous case. Figure 22 shows the estimated 3-D boundary obtained by the proposed algorithm. This figure indicates that while a few internal target points deviate from the actual boundary, most of estimated points are located in close proximity to the true boundaries. The main cause for the decrease in accuracy is that the end of the estimated dielectric boundary
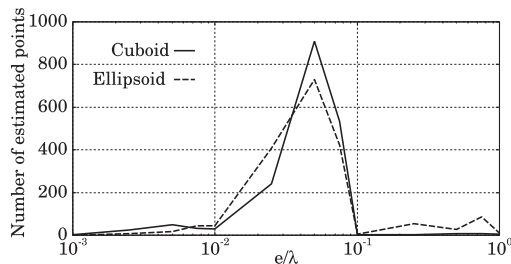

Fig. 23 Number of the estimated target points in each e for the 3-D targets.

deviates slightly from the actual boundary, and causes an error when estimating the propagation path.

Next, to quantitatively analyze the target points obtained using the proposed algorithm, Fig. 23 shows the distribution of estimated points for each value of e$\left(\boldsymbol{q}_{\mathrm{M},i}\right)$, defined in Eq. (7) for both the cuboidal and ellipsoidal dielectric surface. The figure shows that the estimated points in both cases are concentrated around e$\left(\boldsymbol{q}_{\mathrm{M},i}\right) = 5.0 \times 10^{-2}\lambda$.

In addition, the mean value $\bar{e}$ is $4.5 \times 10^{-2}\lambda$ in Fig. 20, and $7.6 \times 10^{-2}\lambda$ in Fig. 22.

Note that the algorithm requires a numerical calculation time of around 14 hours, because the evaluation function introduced in Eq. (8) must evaluate a large number of potential points. The required computational complexity of the proposed algorithm is $O\left(N_X{}^3 N_Y{}^3\right)$, whereas, the conventional SAR-based algorithm requires $O\left(N_X{}^2 N_Y{}^2 N_x N_y N_z\right)$, where N_X, N_Y, N_x, N_y and N_z express the sampling number of X, Y, x, y and z, respectively. Here, we set $N_X = 51$ and $N_Y = 51$. N_x, N_y and N_z are approximately equal to N_X and N_Y. If N_x, N_y and N_z are also set to 51, the computational burden of the proposed algorithm reduces by a factor of 51 compared with the burden of the conventional SAR-based algorithm. As future work, the computational burden must be further decreased to contribute to the design of real-time 3-D imaging sensors such as those to be used in medical screening or non-destructive testing.

7. Conclusion

This paper proposed an accurate and non-parametric imaging algorithm for targets completely buried in a homogeneous dielectric medium and having an arbitrary shape boundary. First, we introduced the extended SAR to internal imaging as a typical conventional algorithm, and stated the problems that it has an enormous computational burden and cannot provide adequate accuracy to identify the detail of the target boundary, including an edge or smooth surface. As a promising solution to these problems, we proposed an accurate imaging algorithm by incorporating the advanced RPM principle and Snell's law. The algorithm has the notable advantage that it exploits accurate boundary points and the normal vectors at the boundary points produced by the RPM algorithm. Through numerical simulations, we have shown that the proposed algorithm achieves less than 1/10 wavelength accuracy for imaging, which is sufficient for determining the detailed structure of the internal target shape. Moreover, it reduced calculation amount for the algorithm 2-D model that was approximately 25 times less than that for the conventional SAR-based algorithm owing to the elimination of the waveform integration for each imaging pixel. It was confirmed that the proposed algorithm extended to the 3-D model by simple modification of the evaluation function in the 2-D model, accomplished non-parametric internal imaging within 1/10 wavelength accuracy. While this algorithm itself does not enhance the spatial resolution of internal imaging, this might be improved by incorporating a super-resolution time of arrival algorithm like MUSIC, or Capon [14] as we intend to in future work.

Furthermore, while this simulation setup assumes non-destructive imaging of the subsurface or concrete wall with respect to the value of permittivity or conductivity, this algorithm can also be applied to biomedical setups such as breast cancer detection, where the contrast between permittivity and conductivity differs from the parameters assumed

in this paper. This is because the proposed algorithm mainly uses an observed range, and if the averaged permittivity is given then the algorithm works by estimating the propagation delay. The permittivity or conductivity contrast between the target and medium mainly involves S/N. In addition, while this paper assumes the near-field case, the proposed algorithm retains its accuracy in both the quasi-far or far field case, provided a sufficient echo from the internal target is obtained. However, for longer range measurements, a greater aperture size is required to obtain a significant target image, as discussed in detail in [11], [12].

References

[1] D.W. Winters, J.D. Shea, E.L. Madsen, G.R. Frank, B.D. Van Veen, and S.C. Hagness, "Estimating the breast surface using UWB microwave monostatic backscatter measurements," IEEE Trans. Biomed. Eng., vol.55, no.1, pp.247–256, Jan. 2008.

[2] Q. Huang, L. Qu, B. Wu, and G. Fang, "UWB through-wall imaging based on compressive sensing," IEEE Trans. Geosci. Remote Sens., vol.48, no.3, pp.1408–1415, March 2010.

[3] A.G. Yarovoy, T.G. Savelyev, P.J. Aubry, P.E. Lys, and L.P. Ligthart, "UWB array-based sensor for near-field imaging," IEEE Trans. Microw. Theory Tech., vol.55, no.6, pp.1288–1295, June 2007.

[4] F. Ahmad, M.G. Amin, and S.A. Kassam, "Synthetic aperture beamformer for imaging through a dielectric wall," IEEE Trans. Aerosp. Electron. Syst., vol.41, no.1, pp.271–283, Jan. 2005.

[5] P. Kosmas and C.M. Rappaport, "A matched-filter FDTD-based time reversal approach for microwave breast cancer detection," IEEE Trans. Antennas Propag., vol.54, no.4, pp.1257–1264, April 2006.

[6] X. Li, E.J. Bond, B.D. Van Veen, and S.C. Hagness, "An overview of ultra-wideband microwave imaging via space-time beamforming for early-stage breast-cancer detection," IEEE Antennas Propag. Mag., vol.47, no.2, pp.19–34, Feb. 2005.

[7] E.J. Bond, X. Li, S.C. Hagness, and B.D. VanVeen, "Microwave imaging via space-time beamforming for early detection of breast cancer," IEEE Trans. Antennas Propag., vol.1, no.8, pp.1690–1705, Aug. 2003.

[8] T. Sakamoto and T. Sato, "A target shape estimation algorithm for pulse radar systems based on boundary scattering transform," IEICE Trans. Commun., vol.E87-B, no.5, pp.1357–1365, May 2004.

[9] S. Kidera, T. Sakamoto, and T. Sato, "A robust and fast imaging algorithm with an envelope of circles for UWB pulse radars," IEICE Trans. Commun., vol.E90-B, no.7, pp.1801–1809, July 2007.

[10] S. Kidera, T. Sakamoto, and T. Sato, "Accurate UWB radar 3-D imaging algorithm for complex boundary without range points connections," IEEE Trans. Geosci. Remote Sens., vol.48, no.48, pp.1993–2004, April 2010.

[11] K. Akune, S. Kidera, and T. Kirimoto, "Acceleration for shadow region imaging algorithm with multiple scattered waves for UWB radars," IEICE Trans. Commun., vol.E94-B, no.9, pp.2696–2699, Sept. 2011.

[12] S. Kidera, T. Sakamoto, and T. Sato, "Extended imaging algorithm based on aperture synthesis with double scattered waves for UWB radars," IEEE Trans. Geosci. Remote Sens., vol.49, no.12, pp.5128–5139, Dec. 2011.

[13] S. Kidera, T. Sakamoto, and T. Sato, "High-resolution and real-time

three-dimensional imaging algorithm with envelopes of spheres for UWB radars," IEEE Trans. Geosci. Remote Sens., vol.46, no.11, pp.3503–3513, Nov. 2008.

[14] S. Kidera, T. Sakamoto, and T. Sato, "Super-resolution UWB radar imaging algorithm based on extended capon with reference signal optimization," IEEE Trans. Antennas Propag., vol.59, no.5, pp.1606–1615, May 2011.

Ken Akune received his B.E. degrees in Electronic Engineering from University of Electro-Communications in 2010. He is currently studying for an M.M. degree at the Graduate School of Informatics and Engineering, University of Electro-Communications. His current research interest is advanced radar signal processing for UWB internal radar systems.

Shouhei Kidera received his B.E. degree in Electrical and Electronic Engineering from Kyoto University in 2003 and M.I. and Ph.D. degrees in Informatics from Kyoto University in 2005 and 2007, respectively. He is an assistant professor in Graduate School of Informatics and Engineering, University of Electro-Communications, Japan. His current research interest is in advanced signal processing for the near field radar, UWB radar. He is a member of the Institute of Electrical and Electronics Engineering (IEEE) and the Institute of Electrical Engineering of Japan (IEEJ).

Tetsuo Kirimoto received the B.S. and M.S. and Ph.D. degrees in Communication Engineering from Osaka University in 1976, 1978 and 1995, respectively. During 1978–2003 he stayed in Mitsubishi Electric Corp. to study radar signal processing. From 1982 to 1983, he stayed as a visiting scientist at the Remote Sensing Laboratory of the University of Kansas. From 2003 to 2007, he joined the University of Kitakyushu as a Professor. Since 2007, he has been with the University of Electro-Communications, where he is a Professor at the Graduate School of Informatics and Engineering. His current study interests include digital signal processing and its application to various sensor systems. Prof. Kirimoto is a senior member of IEEE and a member of SICE (The Society of Instrument and Control Engineers) of Japan.